

# Superionic iron alloys and their seismic velocities in Earth's inner core

<https://doi.org/10.1038/s41586-021-04361-x>

Yu He<sup>1,2,4</sup>✉, Shichuan Sun<sup>1,3,4</sup>, Duck Young Kim<sup>2</sup>, Bo Gyu Jang<sup>2</sup>, Heping Li<sup>1</sup> & Ho-kwang Mao<sup>2</sup>

Received: 13 April 2020

Accepted: 21 October 2021

Published online: 9 February 2022

 Check for updates

Earth's inner core (IC) is less dense than pure iron, indicating the existence of light elements within it<sup>1</sup>. Silicon, sulfur, carbon, oxygen and hydrogen have been suggested to be the candidates<sup>2,3</sup>, and the properties of iron–light-element alloys have been studied to constrain the IC composition<sup>4–19</sup>. Light elements have a substantial influence on the seismic velocities<sup>4–13</sup>, the melting temperatures<sup>14–17</sup> and the thermal conductivities<sup>18,19</sup> of iron alloys. However, the state of the light elements in the IC is rarely considered. Here, using ab initio molecular dynamics simulations, we find that hydrogen, oxygen and carbon in hexagonal close-packed iron transform to a superionic state under the IC conditions, showing high diffusion coefficients like a liquid. This suggests that the IC can be in a superionic state rather than a normal solid state. The liquid-like light elements lead to a substantial reduction in the seismic velocities, which approach the seismological observations of the IC<sup>20,21</sup>. The substantial decrease in shear-wave velocity provides an explanation for the soft IC<sup>21</sup>. In addition, the light-element convection has a potential influence on the IC seismological structure and magnetic field.

Earth's inner core (IC), the central part of our planet, was formed and grown because of the solidification of liquid iron (Fe) alloys in the outer core. Seismological observations suggest that the structure of the IC is complicated and difficult to understand. An unresolved problem is that the IC is soft with a low shear-wave velocity ( $V_s \approx 3.6 \text{ km s}^{-1}$ )<sup>20,21</sup>, which cannot be matched by the sound velocities in Fe and Fe alloys<sup>8–13</sup>. Theoretical predictions have suggested that the premelting effect of Fe and Fe alloys can lead to strong nonlinear shear weakening at high temperatures<sup>22–24</sup>. However, a temperature close to the melting temperature with a small gradient is required. Alternatively, some fractions of melts need to be considered<sup>25</sup>, but the mechanism of the stable presence of the melting fraction since the formation of the IC is unclear. Another long-standing controversy is the reason for the anisotropic seismic velocity structure. In general, the compressional wave velocities ( $V_p$ ) in the polar direction are about 3% larger than those in the equatorial direction in the IC<sup>26</sup>. This phenomenon is explained by the preferred orientation of hexagonal close-packed (hcp) Fe lattices with  $\langle 001 \rangle$  directions<sup>27</sup> or body-centred-cubic (bcc) Fe lattices with  $\langle 111 \rangle$  directions<sup>28</sup> along the spin axis. Moreover, earthquake doublets show that seismic waves have different travel times in the IC over the past few decades. This suggests that the IC structure changes with time, which is attributed to the super-rotation or oscillation of the IC<sup>29–31</sup>. Investigations on the seismic properties of Fe and Fe alloys have improved the understanding of the IC structure. However, direct experimental measurements under the IC conditions are extremely challenging, but ab initio molecular dynamics (AIMD) simulations have increased the knowledge on the properties of Fe alloys<sup>13,22–24,27,28</sup>.

## Superionic Fe alloys

Hydrogen (H), oxygen (O) and carbon (C) are the first, second and fourth most abundant elements in our Solar System, respectively<sup>32</sup>. They are also critical volatiles that have been present in Earth's interior since its formation. In addition, they can be brought down to the core through mantle convection. In hcp-Fe, H and O prefer to take the interstitial site under the IC conditions. For C, recent studies have shown that interstitial C is more stable than substitutional C below about 350 GPa, and that the substitutional structure is stabilized above about 350 GPa, suggesting the coexistence of interstitial and substitutional C under the IC conditions<sup>33,34</sup>. In this study, H, O and C atoms were placed at the interstitial sites of hcp-Fe to verify the light-element effects on the properties of Fe alloys. AIMD simulations were carried out at high pressure–temperature ( $P$ – $T$ ) on  $\text{FeH}_{0.25}$ ,  $\text{FeO}_{0.0625}$  and  $\text{FeC}_{0.0625}$  structures, which contained 0.45 wt%, 1.75 wt% and 1.33 wt% of light elements, respectively. The structures were constructed on the basis of previous experimental studies, and the details are provided in Methods. The solid–superionic–liquid phase transitions with increasing temperature were obtained and are shown in Fig. 1. At low temperatures, light elements in hcp-Fe undergo small mean square displacements (MSDs) and simply vibrate about their lattice positions, demonstrating that the material is an ordinary solid. At temperatures above 3,000 K, the MSDs of light elements increase monotonically with the simulation time, indicating a superionic state, in which the light-element ions become highly diffusive like a liquid (Extended Data Fig. 1). A further increase in temperature leads to the melting of the lattice. The melting temperatures of these structures were estimated using the two-phase

<sup>1</sup>Key Laboratory of High-Temperature and High-Pressure Study of the Earth's Interior, Institute of Geochemistry, Chinese Academy of Sciences, Guiyang, China. <sup>2</sup>Center for High Pressure Science and Technology Advanced Research, Shanghai, China. <sup>3</sup>University of Chinese Academy of Sciences, Beijing, China. <sup>4</sup>These authors contributed equally: Yu He, Shichuan Sun. ✉e-mail: heyu@mail.gyig.ac.cn

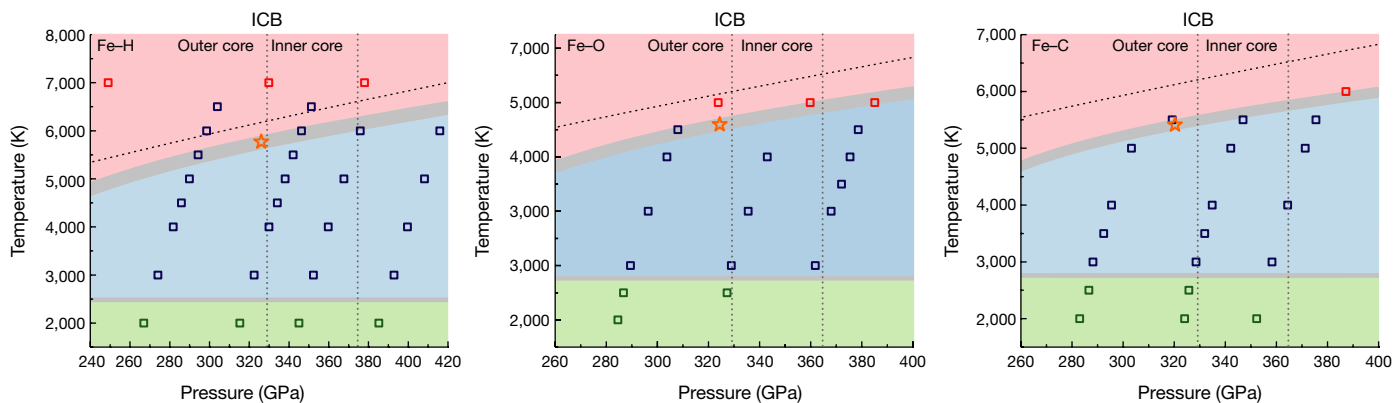


**Fig. 1 | Phase diagrams of  $\text{FeH}_{0.0625}$ ,  $\text{FeO}_{0.0625}$  and  $\text{FeC}_{0.0625}$  at temperatures and pressures in the range of about 2,000–7,000 K and about 250–400 GPa.**

The green, blue and red squares show the solid-state, superionic-state and liquid-state samples in our simulations, respectively. The orange star represents the estimated melting temperature calculated by the two-phase

method. The estimated melting curve is shown by the thick grey curve between the red and blue regions. The blue squares above the melting curves indicate the superheating state. The dashed black curve represents the melting temperatures of pure hcp-Fe from high  $P$ - $T$  experiments<sup>36</sup>. The dashed grey lines show the pressures of the ICB and the central IC.

method to exclude the superheating state in the calculations<sup>35</sup>. The estimated melting temperatures of  $\text{FeH}_{0.0625}$ ,  $\text{FeO}_{0.0625}$  and  $\text{FeC}_{0.0625}$  are approximately 5,770 ( $\pm 200$ ) K, 5,595 ( $\pm 200$ ) K and 5,413 ( $\pm 200$ ) K at about 330 GPa, which are about 500–800 K lower than that of the pure hcp-Fe at the pressure of the inner-core boundary (ICB)<sup>35,36</sup> (Extended Data Fig. 2).

The superionic state is an intermediate state between solid and liquid. Superionic materials have been investigated and are suggested to exist in the interior of Earth and ice giants such as Neptune and Uranus<sup>37–42</sup>. Liquid-like protons in superionic ice may have a significant influence on the magnetic field of these exoplanets<sup>41</sup>. In this study, it is shown that Fe alloys also transform to the superionic state under the IC conditions. Under this condition, H, O and C behave like liquid diffusing within the hcp-Fe lattice. The diffusion coefficients of H, O and C in solid and liquid iron were calculated (Fig. 2). The diffusion coefficients increase markedly with temperature, whereas the effect of pressure is insignificant. Intriguingly, the diffusion coefficients of H, O and C in solid and liquid Fe alloys are nearly identical under the ICB conditions. Although a significant phase transition from liquid to solid in Fe takes place at the ICB, some light elements such as H, O and C still maintain high mobility as fluids in the IC. Therefore, Earth's IC can be viewed as a mixture of solid-like iron and liquid-like light elements, and the convection of light elements continues in it.

The electric conductivities of Fe alloys are important in understanding the energy budget of the geodynamo and the heat flux of Earth's core<sup>18,19</sup>. For superionic Fe alloys, the electric conductivity is composed of ionic conductivity and electronic conductivity. The ionic conductivities were predicted using the Nernst–Einstein equation, and the values are in the range of  $10^2$ – $10^3$  S m<sup>−1</sup> (Extended Data Fig. 3). We also estimated the electronic conductivities using the combination of density functional theory with dynamical mean field theory (DFT + DMFT) method (Extended Data Fig. 4). Although the presence of light elements decreases the electronic conductivity of pure Fe, it is still over two to three orders of magnitude higher than the ionic conductivity; therefore, the conductivity contribution due to the ionic diffusion is negligible.

## Seismic velocities in superionic alloys

The liquid-like light elements in the Fe lattice also affect the seismic velocities. AIMD simulations within the  $NVT$  ( $N$ , number of particles;  $V$ , volume;  $T$ , temperature) ensemble were conducted on  $\text{FeH}_{0.0625}$ ,

$\text{FeO}_{0.0625}$  and  $\text{FeC}_{0.0625}$  at 2,000–6,000 K and 360 GPa. To exclude the effect of the superheating state, the simulation temperatures are lower than the predicted melting temperatures. The structures and cell parameters were carefully determined to maintain hydrostatic stress. The independent elastic constants for  $C_{11}$ ,  $C_{12}$ ,  $C_{13}$ ,  $C_{33}$  and  $C_{44}$  were calculated by distorting the equilibrium structure and solving the stress–strain relations. The compressional ( $V_p$ ) and shear ( $V_s$ ) wave velocities in these structures at high  $P$ - $T$  were deduced from the elastic constants and are plotted in Fig. 3. The  $V_p$  in the alloys decrease almost linearly with temperature, whereas  $V_s$  show an accelerated decline at the solid–superionic transition (Fig. 3c). This suggests that the diffusion of light elements has a significant

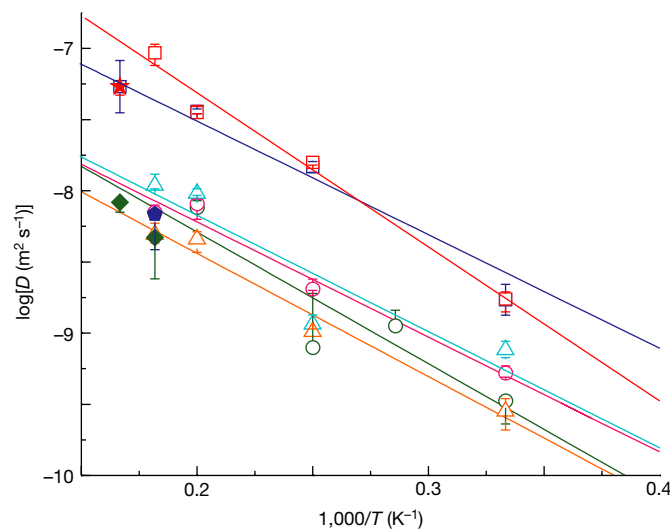


**Fig. 2 | Diffusion coefficients of light elements (H, O and C) in solid and liquid Fe alloys under the IC conditions.** Different diffusion coefficients are shown with different symbols. Blue squares,  $\text{FeH}_{0.0625}$  at about 260 GPa; red squares,  $\text{FeH}_{0.0625}$  at about 360 GPa; cyan triangles,  $\text{FeO}_{0.0625}$  at about 260 GPa; orange triangles,  $\text{FeO}_{0.0625}$  at about 360 GPa; green circles,  $\text{FeC}_{0.0625}$  at about 260 GPa; pink circles,  $\text{FeC}_{0.0625}$  at about 360 GPa. The diffusion coefficients are linearly fitted and shown with coloured lines. The solid red star, green diamonds and blue pentagon represent the diffusion coefficients of H, O and C in liquid Fe at about 330 GPa, respectively. The error bars indicate the variation of linear fitting of MSD data.

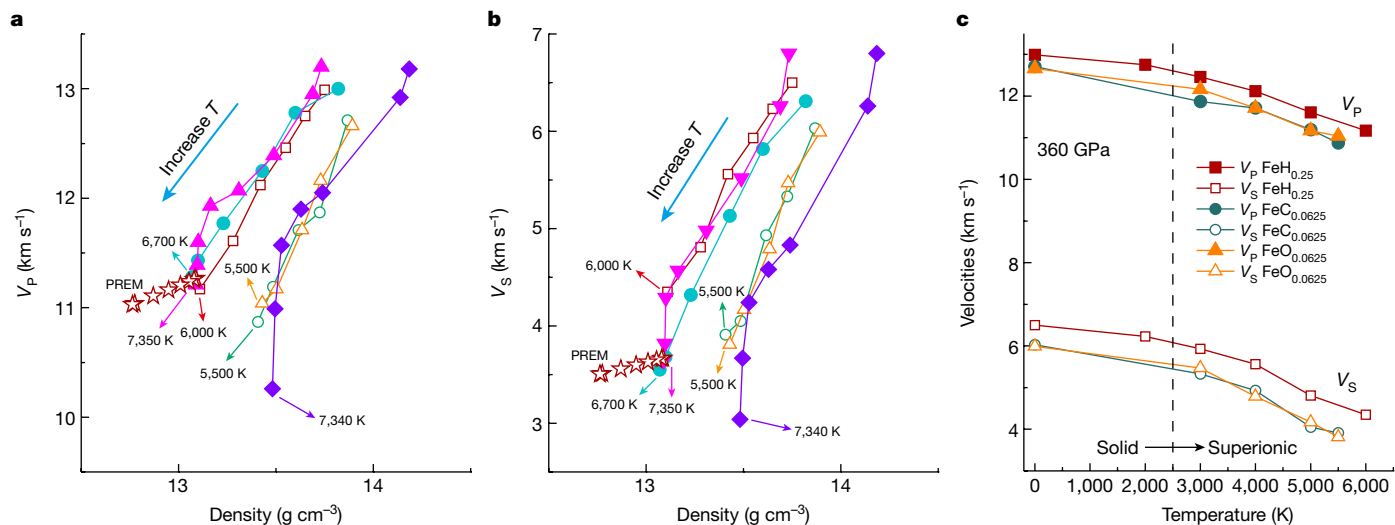


**Fig. 3 | Seismic velocities of  $\text{FeH}_{0.25}$ ,  $\text{FeO}_{0.0625}$  and  $\text{FeC}_{0.0625}$  as a function of density and temperature at 360 GPa.** **a, b**, Calculated compressional-wave velocities ( $V_p$ ; **a**) and shear-wave velocities ( $V_s$ ; **b**) of hcp-Fe alloys compared with the velocities of the PREM in the IC (red stars)<sup>20</sup>. The seismic velocities are compared with the results of previous simulations by different symbols: red open squares,  $\text{FeH}_{0.25}$ ; orange open triangles,  $\text{FeO}_{0.0625}$ ; green open circles,

$\text{FeC}_{0.0625}$ ; purple solid diamonds, Fe (ref.<sup>22</sup>); magenta solid triangles,  $\text{Fe}_{0.9375}\text{Si}_{0.0625}$  (ref.<sup>23</sup>); cyan solid circles,  $\text{Fe}_{60}\text{Si}_2\text{C}_2$  (ref.<sup>24</sup>). The maximum simulation temperatures for different models are labelled. **c**, The evolution of  $V_p$  and  $V_s$  upon the transition from a solid to superionic state with increasing temperature.

effect on  $V_s$ . Owing to this effect, a small amount of diffusive light elements leads to a decrease in seismic velocities and densities, which approach the geophysical observations under the IC conditions. H, O and C superionic light elements have different effects on seismic velocities and densities. A content of 0.45 wt% superionic H in hcp-Fe causes the expected decrease in density. The density of  $\text{FeH}_{0.25}$  at 6,000 K is  $13.12 \text{ g cm}^{-3}$ , which is very close to that of the Preliminary Reference Earth Model (PREM), whereas the presence of diffusive O and C elements has an inconspicuous effect on the density. However, the  $V_s$  in  $\text{FeO}_{0.0625}$  and  $\text{FeC}_{0.0625}$  is lower than that in  $\text{FeH}_{0.25}$  at approximately 5,500 K. Although the  $V_s$  in the Fe alloys are slightly higher than that of the PREM, they may be further reduced when considering the presence of nickel<sup>8</sup>. Poisson's ratio is also an important probe to constrain the composition and structure of the IC. The presence of diffusive light elements also increases Poisson's ratio to 0.41 for H and to 0.43 for C and O, which is quite close to that of the PREM (Extended Data Table 1, Extended Data Fig. 5). Therefore, the superionic Fe alloys at 5,500–6,000 K show similar seismic characteristics to that of the IC. Previous theoretical simulations have shown a decrease in  $V_p$  and  $V_s$  in Fe and Fe alloys with increasing temperature because of the premelting effect<sup>22–24</sup>. However, the calculated velocities are consistent with the PREM at approximately 7,200 K for Fe and at approximately 6,700 K for Fe–Si–C alloy<sup>22,24</sup>, which are higher than the most computationally and experimentally predicted temperatures of the IC<sup>14–19</sup>. Here we provide a mechanism by which highly diffusive light elements lead to significant reductions of  $V_p$  and  $V_s$  close to the PREM model at 5,500–6,000 K. Elastic softening caused by the superionic effect has also been reported in lithium oxide ( $\text{Li}_2\text{O}$ ) at high temperature<sup>43</sup>.

### Superionic inner core

Seismological observations suggest that Earth's core is composed of the liquid outer core with  $V_s$  equal to zero and the solid inner core with  $V_s$  equal to about  $3.6 \text{ km s}^{-1}$ . At the ICB, solidification of the IC generates latent heat and leads to the separation and buoyancy of light-element phases, which promote the convection flows of the

outer core, producing and powering the geomagnetic field (black dashed arrows in Fig. 4). On the basis of our simulations, some interstitial defects such as H, O and C can present in the IC in a superionic state. Owing to the high diffusion coefficients, light elements continue their circulation in the IC (red dashed arrows in Fig. 4). In this case, the IC is not a conventionally known normal solid but a mixture of solid Fe and light-element fluids.

The liquid-like light elements have a significant influence on the elastic properties of the IC, and the long-standing seismic puzzles in the IC, as mentioned above, can be rationalized within the superionic IC model. First, the liquid-like light elements have a profound effect on the seismic velocities, showing  $V_s$  close to that of the PREM at 5,500–6,000 K, which explains why the IC is quite soft. In addition, superionic Fe alloys show 8–11% lower  $V_p$  than that of pure Fe. If the distribution of diffusive light elements in the IC is inhomogeneous with a higher concentration in the equatorial direction than in the polar direction, seismic velocities along the equatorial direction will be lower, which gives a simple reason for the anisotropic seismological structure. Also, the enrichment of liquid-like light elements may enhance seismic wave attenuation, which has been widely observed in the IC<sup>21</sup>. Moreover, the convection of the light elements changes the distribution of the light elements in the IC, leading to the evolution of the seismological structure with time. This phenomenon may provide an alternative interpretation of the different travel times of similar earthquakes<sup>29–31</sup>. In general, the seismic properties of superionic Fe alloys are consistent with the seismological features of the IC.

Some numerical geodynamo models have suggested that the geomagnetic field also has an influence on the IC<sup>44</sup>. In this case, the diffusion of ionic light elements can be affected by the IC magnetic field, and the convection and distribution of light elements may be related to the geometry and the strength of the magnetic field. Furthermore, the seismic velocity in the IC has shown an observable change in the past few decades<sup>29–31</sup>. Therefore, it is important to study whether there is a certain relation between the IC seismic structure and the geomagnetic field, which might be a clue for understanding the structure and evolution of the IC.

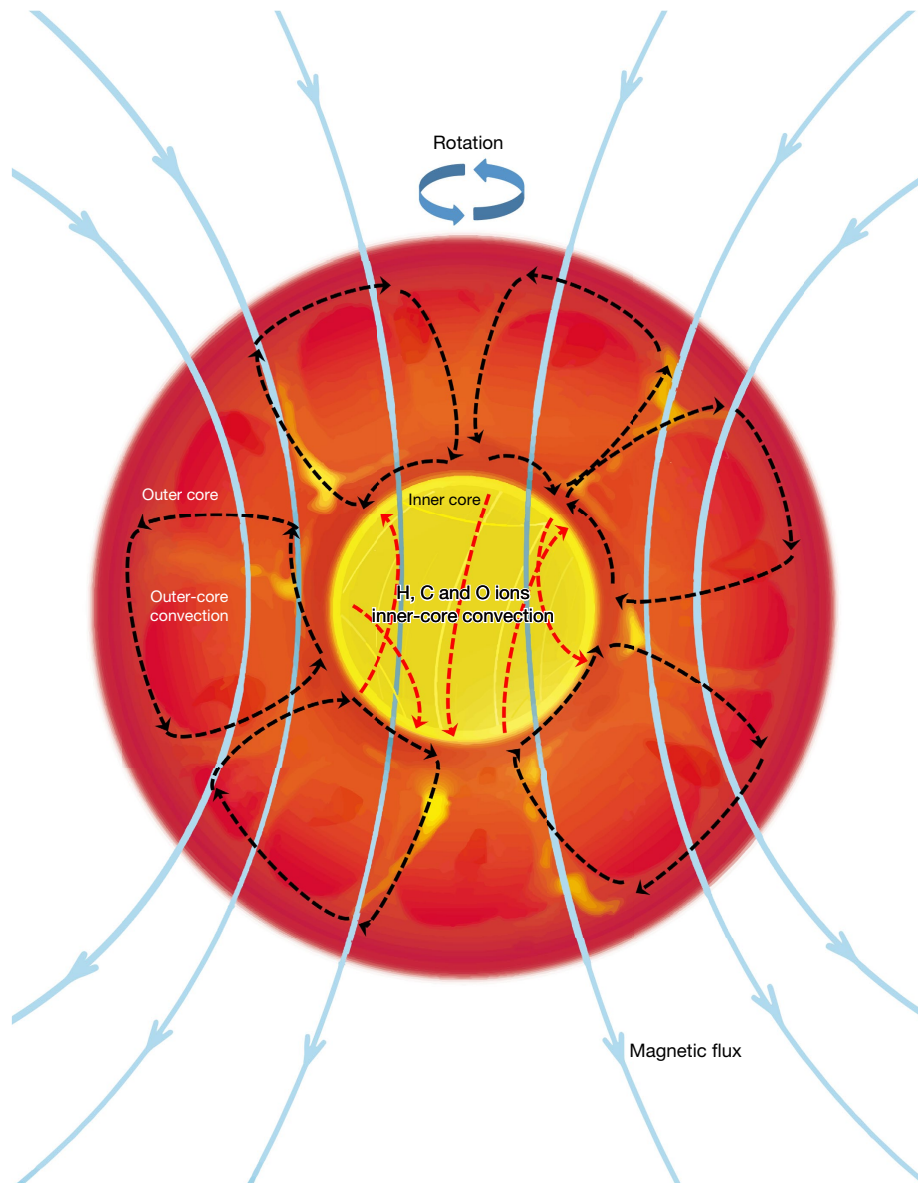


**Fig. 4 | Schematic of the outer-core fluid convection and the IC light-element convection.** The black and red dashed arrow curves represent the outer-core convection generating the geomagnetic field (blue solid curves)

and superionic light-element (H, O and C ions) convection in the IC, respectively.

## Online content

Any methods, additional references, Nature Research reporting summaries, source data, extended data, supplementary information, acknowledgements, peer review information; details of author contributions and competing interests; and statements of data and code availability are available at <https://doi.org/10.1038/s41586-021-04361-x>.

- Birch, F. Elasticity and constitution of the Earth's interior. *J. Geophys. Res.* **57**, 227–286 (1952).
- Poirier, J. P. & Shankland, T. J. Dislocation melting of iron and temperature of the inner core boundary, revisited. *Geophys. J. Int.* **115**, 147–151 (1993).
- Li, J. & Fei, Y. in *Treatise on Geochemistry*, Vol. 2: *The Mantle and Core* (ed. Carlson, R. W.) 1–31 (Elsevier, 2007).
- Li, J., Fei, Y., Mao, H. K., Hirose, K. & Shieh, S. R. Sulfur in the Earth's inner core. *Earth Planet. Sci. Lett.* **193**, 509–514 (2001).
- Badro, J. et al. Effect of light elements on the sound velocity of solid iron: implications for the composition of Earth's core. *Earth Planet. Sci. Lett.* **254**, 233–238 (2007).
- Mao, Z. et al. Sound velocities of Fe and Fe–Si alloy in the Earth's core. *Proc. Natl Acad. Sci. USA* **109**, 10239–10244 (2012).

- Lin, J. F., Heinz, D. L., Campbell, A. J., Devine, J. M. & Shen, G. Y. Iron–silicon alloy in Earth's core? *Science* **295**, 313–315 (2002).
- Lin, J. F. et al. Sound velocities of iron–nickel and iron–silicon alloys at high pressures. *Geophys. Res. Lett.* **30**, 2112 (2003).
- Antonangeli, D. et al. Composition of the Earth's inner core from high-pressure sound velocity measurements in Fe–Ni–Si alloys. *Earth Planet. Sci. Lett.* **295**, 292–296 (2010).
- Chen, B. et al. Hidden carbon in Earth's inner core revealed by shear softening in dense  $\text{Fe}_3\text{C}$ . *Proc. Natl Acad. Sci. USA* **111**, 17755–17758 (2014).
- Prescher, C. et al. High Poisson's ratio of Earth's inner core explained by carbon alloying. *Nat. Geosci.* **8**, 220–223 (2015).
- Shibasaki, Y. et al. Sound velocity measurements in dhcp-FeH up to 70 GPa with inelastic X-ray scattering: implications for the composition of the Earth's core. *Earth Planet. Sci. Lett.* **313–314**, 79–85 (2012).
- Caracas, R. The influence of hydrogen on the seismic properties of solid iron. *Geophys. Res. Lett.* **42**, 3780–3785 (2015).
- Alfè, D., Gillan, M. J. & Price, G. D. Composition and temperature of the Earth's core constrained by combining ab initio calculations and seismic data. *Earth Planet. Sci. Lett.* **195**, 91–98 (2002).
- Terasaki, H. et al. Liquidus and solidus temperatures of a Fe–O–S alloy up to the pressures of the outer core: implication for the thermal structure of the Earth's core. *Earth Planet. Sci. Lett.* **304**, 559–564 (2011).
- Morard, G. et al. Fe–FeO and Fe–Fe<sub>3</sub>C melting relations at Earth's core–mantle boundary conditions: implications for a volatile-rich or oxygen-rich core. *Earth Planet. Sci. Lett.* **473**, 94–103 (2017).

17. Mashino, I., Miozzi, F., Hirose, K., Morard, G. & Sinmyo, R. Melting experiments on the Fe–C binary system up to 255 GPa: constraints on the carbon content in the Earth’s core. *Earth Planet. Sci. Lett.* **515**, 135–144 (2019).
18. Pozzo, M., Davies, C., Gubbins, D. & Alfè, D. Thermal and electrical conductivity of iron at Earth’s core conditions. *Nature* **485**, 355–358 (2012).
19. de Koker, N., Steinle-Neumann, G. & Vlcek, V. Electrical resistivity and thermal conductivity of liquid Fe alloys at high  $P$  and  $T$ , and heat flux in Earth’s core. *Proc. Natl Acad. Sci. USA* **109**, 4070–4073 (2012).
20. Dziewonski, A. M. & Anderson, D. L. Preliminary reference Earth model. *Phys. Earth Planet. Inter.* **25**, 297–356 (1981).
21. Tkalčić, H. & Pham, T.-S. Shear properties of Earth’s inner core constrained by a detection of  $J$  waves in global correlation wavefield. *Science* **362**, 329–332 (2018).
22. Martorell, B., Vočadlo, L., Brodholt, J. & Wood, I. G. Strong premelting effect in the elastic properties of hcp-Fe under inner-core conditions. *Science* **342**, 466–468 (2013).
23. Martorell, B., Wood, I. G., Brodholt, J. & Vočadlo, L. The elastic properties of hcp- $\text{Fe}_{1-x}\text{Si}_x$  at Earth’s inner-core conditions. *Earth Planet. Sci. Lett.* **451**, 89–96 (2016).
24. Li, Y., Vočadlo, L. & Brodholt, J. B. The elastic properties of hcp-Fe alloys under the conditions of the Earth’s inner core. *Earth Planet. Sci. Lett.* **493**, 118–127 (2018).
25. Singh, S. C., Taylor, M. A. J. & Montagner, J. P. On the presence of liquid in Earth’s inner core. *Science* **287**, 2471–2474 (2000).
26. Creager, K. C. Anisotropy of the inner core from differential travel times of the phases PKP and PKIKP. *Nature* **356**, 309–314 (1992).
27. Vočadlo, L., Dobson, D. P. & Wood, I. G. Ab initio calculations of the elasticity of hcp-Fe as a function of temperature at inner-core pressure. *Earth Planet. Sci. Lett.* **288**, 534–538 (2009).
28. Belonosko, A. B., Skorodumova, N. V., Rosengren, A. & Johansson, B. Elastic anisotropy of Earth’s inner core. *Science* **319**, 797–800 (2008).
29. Song, X. & Richards, P. Seismological evidence for differential rotation of the Earth’s inner core. *Nature* **382**, 221–224 (1996).
30. Su, W. J., Dziewonski, A. M. & Jeanloz, R. Planet within a planet: rotation of the inner core of Earth. *Science* **274**, 1883–1887 (1996).
31. Tkalčić, H., Young, M., Bodin, T., Ngo, S. & Sambridge, M. The shuffling rotation of the Earth’s inner core revealed by earthquake doublets. *Nat. Geosci.* **6**, 497–502 (2013).
32. Lodders, K. Solar System abundances and condensation temperatures of the elements. *Astrophys. J.* **591**, 1220–1247 (2003).
33. Li, Y., Vočadlo, L., Alfè, D. & Brodholt, J. B. Carbon partitioning between the Earth’s inner and outer core. *J. Geophys. Res. Solid Earth* **124**, 12812–12824 (2019).
34. Pamato, M. G. et al. Equation of state of hcp Fe–C–Si alloys and the effect of C incorporation mechanism on the density of hcp Fe alloys at 300 K. *J. Geophys. Res. Solid Earth* **125**, e2020JB020159 (2020).
35. Alfè, D. Temperature of the inner-core boundary of the Earth: melting of iron at high pressure from first-principles coexistence simulations. *Phys. Rev. B* **79**, 060101 (2009).
36. Anzellini, S., Dewaele, A., Mezouar, M., Loubeyre, P. & Morard, G. Melting of iron at Earth’s inner core boundary based on fast X-ray diffraction. *Science* **340**, 464–466 (2013).
37. Cavazzoni, C. et al. Superionic and metallic states of water and ammonia at giant planet conditions. *Science* **283**, 44–46 (1999).
38. Goldman, N., Fried, L. E., Kuo, I.-F. W. & Mundy, C. J. Bonding in the superionic phase of water. *Phys. Rev. Lett.* **94**, 217801 (2015).
39. Hernandez, J.-A. & Caracas, R. Superionic–superionic phase transitions in body-centered cubic  $\text{H}_2\text{O}$  ice. *Phys. Rev. Lett.* **117**, 135503 (2016).
40. Millot, M. et al. Nanosecond X-ray diffraction of shock-compressed superionic water ice. *Nature* **569**, 251–255 (2019).
41. Millot, M. et al. Experimental evidence for superionic water ice using shock compression. *Nat. Phys.* **14**, 297–302 (2018).
42. Hou, M. et al. Superionic iron oxide–hydroxide in Earth’s deep mantle. *Nat. Geosci.* **14**, 174–178 (2021).
43. Hull, S., Farley, T. W. D., Hayes, W. & Hutchings, M. T. The elastic properties of lithium oxide and their variation with temperature. *J. Nucl. Mater.* **160**, 125–134 (1988).
44. Glatzmaier, G. A. & Roberts, P. H. Rotation and magnetism of Earth’s inner core. *Science* **274**, 1887–1891 (1996).

**Publisher’s note** Springer Nature remains neutral with regard to jurisdictional claims in published maps and institutional affiliations.

© The Author(s), under exclusive licence to Springer Nature Limited 2022

## Methods

### Model construction and thermodynamic stability

The stable phase of Fe under Earth's IC conditions is still controversial. Both hcp-Fe and bcc-Fe are considered as candidates for the main phase in the IC<sup>45,46</sup>. Here we chose hcp-Fe alloys as the simulation models because recent experimental and computational studies have suggested that hcp-Fe alloys show seismic velocities close to the PREM under the IC conditions<sup>13,22–24,47–49</sup>.

The light-element impurities may take substitutional and/or interstitial sites in hcp-Fe. Therefore, the relative thermodynamic stability of H, O, C, S and Si at interstitial sites are investigated at 360 GPa and 0 K. We consider the stability of interstitial defects in binary (Fe–X) Fe alloys (X = H, O, C, S and Si). A  $4 \times 4 \times 2$  supercell containing 64 Fe atoms was used for the calculation. A substitutional defect ( $X^s$ ) was generated by replacing an Fe atom and an interstitial defect ( $X^i$ ) was generated by adding an X atom at the octahedral interstitial site. When  $X^s$  and  $X^i$  coexisted (Fe– $X^s$ – $X^i$ ), both correlated (dimer) and separated (substitutional + interstitial) configurations are considered. Geometry optimizations were performed at 360 GPa using conjugate gradients minimization until all of the forces acting on the ions were less than 0.01 eV Å<sup>-1</sup> per atom. A  $3 \times 3 \times 4$  k-point mesh was adopted. The chemical potential of the distinctive element X in hcp-Fe was calculated by

$$\mu_X = \frac{H(Fe_N X_M) - H(Fe_N)}{M},$$

where  $N$  and  $M$  are the number of Fe and light-element atoms in the structure. As shown in Extended Data Fig. 6, H at interstitial sites is energetically much more favourable, which is consistent with previous experimental and computational results<sup>13,50</sup>. We also conducted AIMD simulations on the substitution H model (Fe<sub>60</sub>H<sub>4</sub>) at 360 GPa and 5,000 K, and found the obvious diffusion of Fe atoms, which suggests that this structure is not stable (Extended Data Fig. 7a). Substitutional structures are more stable for Fe–S and Fe–Si alloys. For C and O, the dimer structure is the most stable, indicating the coexistence of substitutional and interstitial defects. Li et al.<sup>33</sup> investigated the stability of Fe–C alloys at high temperature using the quasiharmonic approximation (QHA) method, and they found that the stability of the dimer structure is weakened and its relative free energy is slightly higher than that of the substitutional structure at 6,500 K. A recent study from the same group suggested that the interstitial C becomes thermodynamically more stable than substitutional C at pressures below about 350 GPa (ref. <sup>34</sup>). The stability of interstitial C in hcp-Fe at 340 GPa is further confirmed by QHA calculations, and O is also more stable at interstitial sites at 360 GPa and temperatures up to 6,000 K (Extended Data Fig. 7).

The QHA thermodynamics calculations were performed using Phonopy code adopting over ten fully relaxed structures with different volumes<sup>51</sup>. The Gibbs free energy was calculated by

$$G(V, T) = U(V) + F_{ph}(V, T) + F_{el}(V, T) - TS_{conf} + PV,$$

where  $U(V)$  is the static internal energy,  $F_{ph}(V, T)$  is the energy contribution of vibrations:

$$F_{ph}(V, T) = \sum_{q,i} \left[ \frac{1}{2} \hbar \omega_{q,i} + k_B T \ln \left( 1 - e^{-\frac{\hbar \omega_{q,i}}{k_B T}} \right) \right],$$

where  $\hbar$  and  $k_B$  are the Planck constant and Boltzmann constant, respectively,  $\omega_{q,i}$  is the vibrational frequency of the  $i$ th mode at the  $q$  point and  $T$  is temperature.

$F_{el}(V, T)$  is the electronic contribution to the free energy, which should be taken into account for metals.

$$F_{el}(V, T) = \gamma \sum_i f(\varepsilon_i, T) - TS_{el}(V, T),$$

With the electronic entropy given by

$$S_{el}(V, T) = -\gamma k_B \sum_i [f(\varepsilon_i, T) \ln f(\varepsilon_i, T) + (1-f(\varepsilon_i, T)) \ln (1-f(\varepsilon_i, T))],$$

where  $\gamma$  is 1 or 2 for collinear spin polarized and non-spin polarized systems, respectively, the Fermi–Dirac distributions  $f(\varepsilon_i, T)$  are computed as function of the energies  $\varepsilon_i$  from the electronic density of states. For defective systems, the configurational entropy  $S_{conf}$  is estimated by

$$S_{conf} = -k_B [X \ln X + (1-X) \ln (1-X)],$$

where  $X$  is the defect concentration.

$G(V, T)$  can be transformed to  $G(P, T)$  by minimizing the free energy with respect to volume at a constant pressure, and the relative defect formation energy of hcp-Fe was calculated by

$$\Delta G(P, T) = \frac{2G(Fe) + G(Fe_{62}X_2)_{sub} - G(Fe_{64}X_2)_{int}}{2}.$$

It is worth noting that extra entropy contributed by the highly diffusive light elements at interstitial sites, which is not considered in QHA calculations, may further stabilize the superionic structure at high temperature<sup>40,52</sup>.

Regarding the concentration of light-element defects, H is known to be soluble in solid Fe at high  $P-T$  with the concentration over about 1 wt% (refs. <sup>12,53</sup>). The solubility of C in hcp-Fe is about 1 wt% at about 211 GPa (ref. <sup>17</sup>), whereas the O concentration in solid Fe can be negligible<sup>54</sup>. However, Si and S can form solid solution in hcp-Fe with high concentrations up to about 16% for Si and about 5% for S (refs. <sup>48,55–57</sup>). On the basis of the solubility, light-element bearing hcp-Fe structures were constructed by locating one H, O, C, Si and S atom at the central site of hcp-Fe supercells ( $2 \times 1 \times 1$  supercell for H and  $2 \times 2 \times 1$  supercell for O, C, Si and S). The light-element concentration in the Fe<sub>16</sub>H, Fe<sub>16</sub>O, Fe<sub>16</sub>C, Fe<sub>16</sub>Si and Fe<sub>16</sub>S structures is 0.45 wt%, 1.75 wt%, 1.33 wt%, 3.04 wt% and 3.46 wt%, respectively. Although the solubility of O in hcp-Fe might be very low under the IC conditions, we still study the Fe<sub>16</sub>O structure and the result will benefit the understanding of O defects in hcp-Fe. The structure relaxations were performed using the Perdew–Burke–Ernzerhof exchange-correlation functional and projector augmented wave (PAW) method<sup>58</sup> as implemented in the Vienna Ab initio Simulation Package (VASP)<sup>59</sup>. In our calculations, a plane-wave representation for the wavefunction with a cut-off energy of 800 eV was adopted. Geometry optimizations were performed at pressures from about 250 GPa to about 360 GPa using conjugate gradients minimization until all of the forces acting on the ions were less than 0.01 eV Å<sup>-1</sup> per atom. A  $k$ -point mesh with a spacing of about 0.03 Å<sup>-1</sup> was used.

### Solid–superionic–liquid phase transition and ionic transport property

The solid–superionic–liquid phase transitions for the structures under the IC conditions were investigated by AIMD. The AIMD method has been widely used to simulate the ionic conductivity<sup>60,61</sup>, the melting temperature<sup>35</sup>, the phase transition<sup>39,62,63</sup> and the elastic properties<sup>13,22–24,27</sup> of materials at high  $P-T$ . Here enlarged supercells for Fe<sub>64</sub>H<sub>16</sub>, and Fe<sub>64</sub>X<sub>4</sub> (X = O, C, Si and S) were used for AIMD simulation. It is worth noting that a bigger supercell containing 128 Fe atoms and 32 H atoms or 8 X (X = O, C, Si and S) atoms did not change the simulation results. The simulations used the canonical ensemble ( $NVT$ ) with a time step of 1 fs. The simulations lasted about 10–100 ps at temperatures from about 2,000 K to about 7,000 K and pressures from about 250 GPa to about 400 GPa. The MSD:

$$\langle [\mathbf{r}(t)]^2 \rangle = \frac{1}{N} \sum_{i=1}^N \langle [\mathbf{r}_i(t+t_0) - \mathbf{r}_i(t_0)]^2 \rangle$$

is averaged over specific ions, and  $\mathbf{r}_i(t)$  is the displacement of the  $i$ th ion at time  $t$ , and  $N$  is the total number of specific ions in the system. For  $\text{Fe}_{64}\text{Si}_4$  and  $\text{Fe}_{64}\text{S}_4$  alloys, we did not observe a superionic transition—the structures transfer directly to a liquid state at about 3,000 K and about 330 GPa (Extended Data Fig. 8). This suggests that the  $\text{Fe}_{64}\text{Si}_4$  and  $\text{Fe}_{64}\text{S}_4$  alloys are not stable under the IC conditions. The diffusion coefficients and ionic conductivities were calculated using the MSD. The detailed methods are provided in our previous reports<sup>42,61</sup>.

### Melting temperature prediction using the two-phase method

During AIMD simulations, a superheating solid state is obtained above the melting temperature ( $T_m$ )<sup>64</sup>. To exclude the influence of the superheating state, the melting temperatures of these alloys should be estimated. Considering the influence of the light-element partition between the solid phase and the liquid phase<sup>65</sup>, we used a coexisting solid and liquid system, which is also known as the two-phase method<sup>66–69</sup>, to predict the melting temperature.

The two-phase method has been widely used to predict the melting temperatures of different materials such as metals<sup>66</sup>, hydrogen<sup>67</sup>, lithium hydride<sup>68</sup> and oxides<sup>69</sup>. Under a constant internal energy, a coexisting two-phase system can be maintained for a period of time, and the average temperature of the coexisting system denotes a melting point. A simulated structure was generated by combining a solid and liquid Fe-light-element structure. The solid structures were obtained from the structures of  $\text{FeH}_{0.25}$ ,  $\text{FeO}_{0.0625}$  and  $\text{FeC}_{0.0625}$  at 360 GPa and 6,000 K, 5,500 K and 5,500 K, respectively. The liquid structures were generated by heating the solid structures at about 9,000 K for about 2 ps, and then slowly cooling to about 6,000 K. The simulations were performed in the  $NVE$  ( $N$ , number of particles;  $V$ , volume;  $E$ , internal energy) ensemble using supercells with different volumes containing 256 Fe atoms and 64, 16 and 16 atoms of H, O and C, respectively. The cut-off energy was set to 400 eV with the  $\Gamma$  point for  $k$ -space sampling. The time step was set at 1 fs with total simulation of over 12 ps. The two-phase coexisting states were maintained during our simulation (Extended Data Fig. 9). The pressures and temperatures in these simulations are shown in Extended Data Fig. 2, and the average melting temperatures for  $\text{FeH}_{0.25}$ ,  $\text{FeO}_{0.0625}$  and  $\text{FeC}_{0.0625}$  are approximately 5,770 ( $\pm 200$ ) K, 5,595 ( $\pm 200$ ) K and 5,413 ( $\pm 200$ ) K at 324.4 ( $\pm 1.0$ ) GPa, 320.3 ( $\pm 1.0$ ) GPa and 324.3 ( $\pm 1.0$ ) GPa, respectively. Compared with previous experimental<sup>36,70</sup> and computational<sup>66,71,72</sup> studies, these fluid-like impurities also reduce the melting temperature by about 500–1,000 K. We also observed the diffusion of H, O and C in solid phases, and the interdiffusion of the light elements between the liquid and solid phases. Thus, the superionic effect should be considered when calculating the light-element partition at the ICB. The computational results are in agreement with the results of previous experimental studies<sup>12,16,17</sup> (Supplementary Fig. 1). Accordingly, the estimated melting temperatures of  $\text{FeH}_{0.25}$ ,  $\text{FeO}_{0.0625}$  and  $\text{FeC}_{0.0625}$  are approximately within 5,500–6,000 K, and simulation temperatures of our further studies on elastic properties are constrained below the melting temperatures.

### DFT + DMFT calculations and electronic conductivities

To estimate the electronic conductivity of Fe,  $\text{FeH}_{0.25}$ ,  $\text{FeO}_{0.0625}$  and  $\text{FeC}_{0.0625}$ , we considered the resistivity from electron-electron scattering ( $\rho_{e-e}$ ) and electron-phonon scattering ( $\rho_{e-ph}$ ). The  $\rho_{e-e}$  of Fe and Fe alloys were calculated by using DFT + DMFT as implemented in the WIEN2k + eDMFT package (<http://hauleweb.rutgers.edu/tutorials/>)<sup>73</sup>. We used the volume obtained from AIMD calculation at about 5,500–6,000 K in the DFT + DMFT calculation to include the volume expansion effect on the electronic conductivity. Perdew–Burke–Ernzerhof generalized gradient approximation was used for the exchange-correlation functional<sup>74</sup>.

The correlation effect of the Fe 3d orbital was treated dynamically by local self-energy in the DMFT part on the top of an effective one-electron Hamiltonian generated from the DFT part. A 1,000  $k$ -points mesh was used in the DFT + DMFT self-consistent calculation. We used the Coulomb interaction  $U=5$  eV and Hund's coupling  $J=0.943$  eV, which is consistent with a previous theoretical study on hcp-Fe<sup>75</sup>. The local impurity problem was solved by using continuous-time quantum Monte Carlo impurity solver. A 7,000  $k$ -point mesh was used for the conductivity calculation based on the self-energy obtained from the self-consistent calculation with a 1,000  $k$ -points mesh.

As the unit cells of Fe alloys are too large to calculate  $\rho_{e-ph}$  in a first-principles manner, we took a previously calculated result for hcp-Fe by using the density functional perturbation theory and Boltzmann transport theory<sup>75</sup>. Therefore, the total resistivity was given by the sum of  $\rho_{e-e}$  calculated from DFT + DMFT and the reported  $\rho_{e-ph}$  of hcp-Fe. Then, the electronic conductivities of Fe and Fe alloys were obtained. Considering the alloy effect on the  $\rho_{e-ph}$  part, the electronic conductivity of Fe alloys ( $\text{FeH}_{0.25}$ ,  $\text{FeO}_{0.0625}$  and  $\text{FeC}_{0.0625}$ ) can decrease further by roughly 10% (ref. <sup>19,76</sup>).

### AIMD simulations on the elastic properties

The elastic properties are calculated using the AIMD method, which has been used in our previous studies<sup>77,78</sup>. We constructed structures for hcp-Fe with C, H and O light elements in  $4 \times 4 \times 2$  supercells at 2,000–6,000 K and 360 GPa. We determined the equilibrium volume and cell parameters at different temperatures by conducting a grid of  $NVT$  ensemble simulations over volumes and temperatures using a Nosé thermostat<sup>79</sup>. For each equilibrium structure of different temperatures, a 10,000-time-steps (10 ps) simulation was calculated to check that the stress field is hydrostatic. The elastic constant  $C_{ij}$  ( $i$  and  $j=1, 2, 3, 4, 5, 6$ ) was calculated by distorting the equilibrium structure and solving the stress-strain relations.

The elastic properties of crystal are expressed as the relationship between stress and strain:

$$\begin{pmatrix} \sigma_1 \\ \sigma_2 \\ \sigma_3 \\ \sigma_4 \\ \sigma_5 \\ \sigma_6 \end{pmatrix} = \begin{pmatrix} C_{11} & C_{12} & C_{13} & C_{14} & C_{15} & C_{16} \\ C_{21} & C_{22} & C_{23} & C_{24} & C_{25} & C_{26} \\ C_{31} & C_{32} & C_{33} & C_{34} & C_{35} & C_{36} \\ C_{41} & C_{42} & C_{43} & C_{44} & C_{45} & C_{46} \\ C_{51} & C_{52} & C_{53} & C_{54} & C_{55} & C_{56} \\ C_{61} & C_{62} & C_{63} & C_{64} & C_{65} & C_{66} \end{pmatrix} \begin{pmatrix} \varepsilon_1 \\ \varepsilon_2 \\ \varepsilon_3 \\ \varepsilon_4 \\ \varepsilon_5 \\ \varepsilon_6 \end{pmatrix}.$$

For the hexagonal system investigated in this study, we calculated the five non-equivalent elastic constants,  $C_{11}$ ,  $C_{12}$ ,  $C_{13}$ ,  $C_{33}$  and  $C_{44}$ .  $C_{11}$ ,  $C_{12}$  and  $C_{13}$  can be obtained by the strain tensor:

$$\varepsilon = \begin{pmatrix} \delta & 0 & 0 \\ 0 & 0 & 0 \\ 0 & 0 & 0 \end{pmatrix}.$$

We obtained  $C_{33}$  using the strain tensor:

$$\varepsilon = \begin{pmatrix} 0 & 0 & 0 \\ 0 & 0 & 0 \\ 0 & 0 & \delta \end{pmatrix},$$

and we obtained  $C_{44}$  using the strain tensor:

$$\varepsilon = \begin{pmatrix} 0 & 0 & 0 \\ 0 & 0 & \delta/2 \\ 0 & \delta/2 & 0 \end{pmatrix},$$

where  $\delta$  is the magnitude of distortion. For  $\delta$  of  $\pm 0.01$ ,  $\pm 0.005$  and 0, five group of strains were added by:

$$a' = a(I + \varepsilon),$$

where  $a$  represents a  $3 \times 3$  cell parameter matrix,  $\varepsilon$  represents the added strain  $\Delta\varepsilon$ , and  $I$  represents a  $3 \times 3$  identity matrix. Then we obtained an elastic moduli through dealing with the stress–strain relationship. To ensure the reliability and full convergence of the results, 10,000 time steps of  $NVT$  simulations were carried out for each distorted direction. The final results of the strain–stress data show a good linear relationship and were fitted using the central difference method. The calculated  $C_{ij}$  results satisfy Born's stability conditions:

$$C_{11} > |C_{12}|, (C_{11} + C_{12})C_{33} > 2C_{13}^2, C_{44} > 0, C_{66} > 0.$$

We calculated the bulk  $B$  and shear  $G$  moduli using the Voigt average scheme, which proved more appropriate and accurate in calculating the seismic wave properties.

The primary wave velocity  $V_p$ , shear wave velocity  $V_s$  and bulk sound velocity  $V_\phi$  are:

$$V_p = \sqrt{\frac{B + \frac{4G}{3}}{\rho}}, V_s = \sqrt{\frac{G}{\rho}}, V_\phi = \sqrt{\frac{B}{\rho}}.$$

Poisson's ratio was calculated by:

$$\nu = \frac{3B - G}{2(3B + G)},$$

We calculated the elastic constants of pure Fe at 360 GPa, and the validity of this method was confirmed by comparison with previously reported data (Supplementary Fig. 2)<sup>22</sup>. The convergence tests confirmed that a larger supercell and longer simulation time do not change our results for the elastic constants and the diffusion coefficients (Supplementary Figs. 3, 4, Supplementary Table 1).

## Data availability

The data supporting the findings of this study have been deposited at the 4TU Center for Research Data: <https://doi.org/10.4121/12932588.v2>. Any additional data are available upon request from the corresponding author. Source data are provided with this paper.

## Code availability

The Vienna Ab initio Simulation Package is a proprietary software available for purchase at <https://www.vasp.at/>. Phonopy code is available at <http://phonopy.github.io/phonopy/>. WIEN2k is available at <http://www.wien2k.at/>. The WIEN2k+eDMFT package is available at <http://hauleweb.rutgers.edu/tutorials/>.

45. Tateno, S., Hirose, K., Ohishi, Y. & Tatsumi, Y. The structure of iron in Earth's inner core. *Science* **330**, 359–361 (2010).
46. Belonoshko, A. B., Rajeev, A. & Johansson, B. Stability of the body-centred-cubic phase of iron in the Earth's inner core. *Nature* **424**, 1032–1034 (2003).
47. Sakamaki, T. et al. Constraints on Earth's inner core composition inferred from measurements of the sound velocity of hcp-iron in extreme conditions. *Sci. Adv.* **2**, e1500802 (2016).
48. Antonangeli, D. et al. Sound velocities and density measurements of solid hcp-Fe and hcp-Fe–Si (9 wt.%) alloy at high pressure: constraints on the Si abundance in the Earth's inner core. *Earth Planet. Sci. Lett.* **482**, 446–453 (2018).
49. Caracas, R. The influence of carbon on the seismic properties of solid iron. *Geophys. Res. Lett.* **44**, 128–134 (2017).
50. Tagawa, S., Ohta, K., Hirose, K., Kato, C. & Ohishi, Y. Compression of Fe–Si–H alloys to core pressures. *Geophys. Res. Lett.* **43**, 3686–3692 (2016).
51. Togo, A. & Tanaka, I. First principles phonon calculations in materials science. *Scr. Mater.* **108**, 1–5 (2015).
52. Klarbring, J. & Simak, S. I. Phase stability of dynamically disordered solids from first principles. *Phys. Rev. Lett.* **121**, 225702 (2018).
53. Terasaki, H. et al. Stability of Fe–Ni hydride after the reaction between Fe–Ni alloy and hydrous phase ( $\delta$ -AlOOH) up to 1.2 Mbar: possibility of H contribution to the core density deficit. *Phys. Earth Planet. Inter.* **194–195**, 18–24 (2012).
54. Ozawa, H., Hirose, K., Tateno, S., Sata, N. & Ohishi, Y. Phase transition boundary between B1 and B8 structures of FeO up to 210 GPa. *Phys. Earth Planet. Inter.* **179**, 157–163 (2010).
55. Tateno, S., Kuwayama, Y., Hirose, K. & Ohishi, Y. The structure of Fe–Si alloy in Earth's inner core. *Earth Planet. Sci. Lett.* **418**, 11–19 (2015).
56. Mori, Y. et al. Melting experiments on Fe–Fe<sub>3</sub>S system to 254 GPa. *Earth Planet. Sci. Lett.* **464**, 135–141 (2017).
57. Fischer, R. A. et al. Equation of state and phase diagram of Fe–16Si alloy as a candidate component of Earth's core. *Earth Planet. Sci. Lett.* **357–358**, 268–276 (2012).
58. Blöchl, P. E. Projector augmented-wave method. *Phys. Rev. B* **50**, 17953–17979 (1994).
59. Kresse, G. Efficient iterative schemes for ab initio total-energy calculations using a plane-wave basis set. *Phys. Rev. B* **54**, 11169–11186 (1996).
60. Alfè, D. & Gillan, M. J. First-principles calculation of transport coefficients. *Phys. Rev. Lett.* **81**, 5161–5164 (1998).
61. He, Y. et al. First-principles prediction of fast migration channels of potassium ions in  $KAlSi_3O_8$  hollandite: implications for high conductivity anomalies in subduction zones. *Geophys. Res. Lett.* **43**, 6228–6233 (2016).
62. Mookherjee, M., Stixrude, L. & Karki, B. Hydrous silicate melt at high pressure. *Nature* **452**, 983–986 (2008).
63. Belonoshko, A. B. et al. Stabilization of body-centred cubic iron under inner-core conditions. *Nat. Geosci.* **10**, 312–316 (2017).
64. Alfè, D., Cazorla, C. & Gillan, M. J. The kinetics of homogeneous melting beyond the limit of superheating. *J. Chem. Phys.* **135**, 024102 (2011).
65. Alfè, D., Gillan, M. J. & Price, G. D. Temperature and composition of the Earth's core. *Contemp. Phys.* **48**, 63–80 (2007).
66. Alfè, D. First-principles simulations of direct coexistence of solid and liquid aluminum. *Phys. Rev. B* **68**, 064423 (2003).
67. Bonev, S. A., Schwegler, E., Ogitsu, T. & Galli, G. A quantum fluid of metallic hydrogen suggested by first-principles calculations. *Nature* **431**, 669–672 (2004).
68. Ogitsu, T., Schwegler, E., Gygi, F. & Galli, G. Melting of lithium hydride under pressure. *Phys. Rev. Lett.* **91**, 175502 (2003).
69. Alfè, D. Melting curve of MgO from first-principles simulations. *Phys. Rev. Lett.* **94**, 235701 (2005).
70. Yoo, C. S., Holmes, N. C., Ross, M., Webb, D. J. & Pike, C. Shock temperatures and melting of iron at Earth core conditions. *Phys. Rev. Lett.* **70**, 3931–3934 (1993).
71. Alfè, D., Price, G. D. & Gillan, M. J. Iron under Earth's core conditions: liquid-state thermodynamics and high-pressure melting curve from ab initio calculations. *Phys. Rev. B* **65**, 165118 (2002).
72. Sola, E. & Alfè, D. Melting of iron under Earth's core conditions from diffusion Monte Carlo free energy calculations. *Phys. Rev. Lett.* **103**, 078501 (2009).
73. Haule, K., Yee, C.-H. & Kim, K. Dynamical mean-field theory within the full-potential methods: electronic structure of CeIrIn<sub>5</sub>, CeCoIn<sub>5</sub>, and CeRhIn<sub>5</sub>. *Phys. Rev. B* **81**, 195107 (2010).
74. Perdew, J. P., Burke, K. & Ernzerhof, M. Generalized gradient approximation made simple. *Phys. Rev. Lett.* **78**, 1396 (1997).
75. Xu, J. et al. Thermal conductivity and electrical resistivity of solid iron at Earth's core conditions from first principles. *Phys. Rev. Lett.* **121**, 096601 (2018).
76. Gomi, H. et al. The high conductivity of iron and thermal evolution of the Earth's core. *Phys. Earth Planet. Inter.* **224**, 88–103 (2013).
77. Sun, S., He, Y., Kim, D. Y. & Li, H. Anomalous elastic properties of superionic ice. *Phys. Rev. B* **102**, 104108 (2020).
78. He, Y., Sun, S. & Li, H. Ab initio molecular dynamics investigation of the elastic properties of superionic  $Li_2O$  under high temperature and pressure. *Phys. Rev. B* **103**, 174105 (2021).
79. Nosé, S. A unified formulation of the constant temperature molecular dynamics methods. *J. Chem. Phys.* **81**, 511–519 (1984).

**Acknowledgements** This study was supported by the Strategic Priority Research Program (B) of the Chinese Academy of Sciences (XDB 18010401). We acknowledge the support of the National Natural Science Foundation of China (42074104, 41774101, 11774015, U1930401) and the Youth Innovation Promotion Association of CAS (2020394). Numerical computations were performed at the Hefei Advanced Computing Center, the Shanghai Supercomputer Center and the National Supercomputer Center in Guangzhou.

**Author contributions** Y.H. and S.S. contributed equally to this work, conducted the calculations, analysed the data and wrote the manuscript. Y.H., D.Y.K. and H.-k.M. initiated and designed the project. Y.H. conducted calculations on phase transition, melting temperatures and diffusion properties. S.S. performed simulations on elastic properties. B.G.J. performed electronic conductivity calculations. Y.H., D.Y.K. and H.L. discussed the geophysical implications. All authors discussed the data interpretation and commented on the manuscript.

**Competing interests** The authors declare no competing interests.

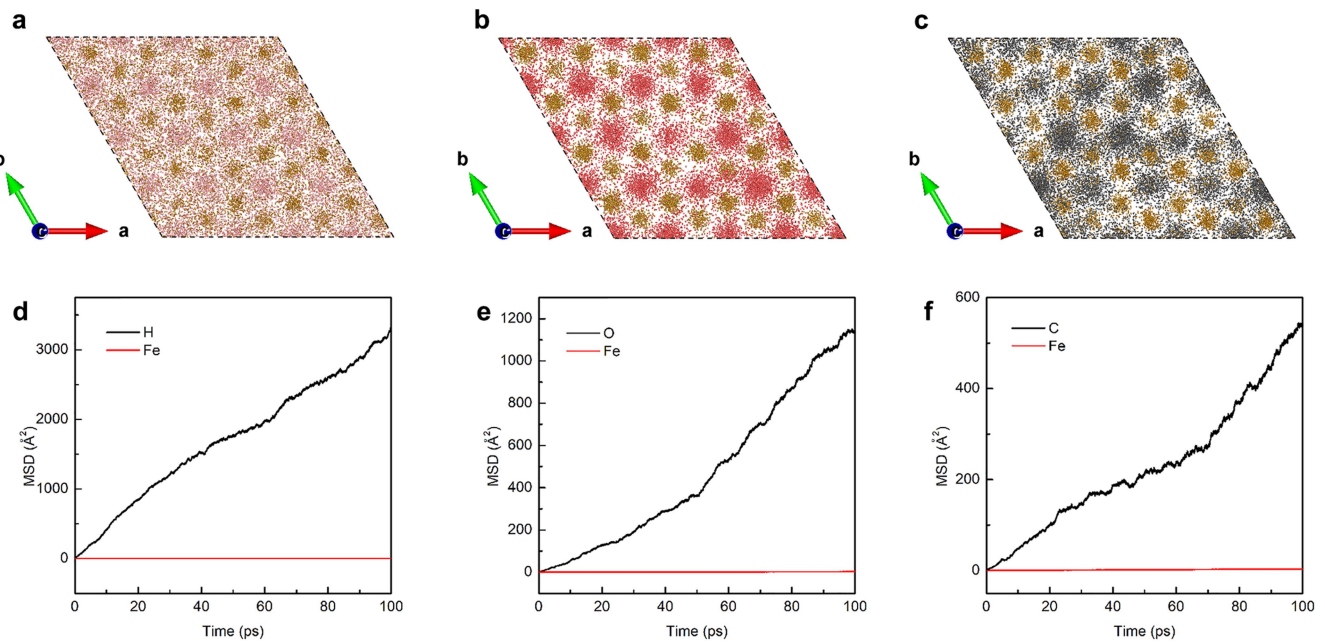
## Additional information

**Supplementary information** The online version contains supplementary material available at <https://doi.org/10.1038/s41586-021-04361-x>.

**Correspondence and requests for materials** should be addressed to Yu He.

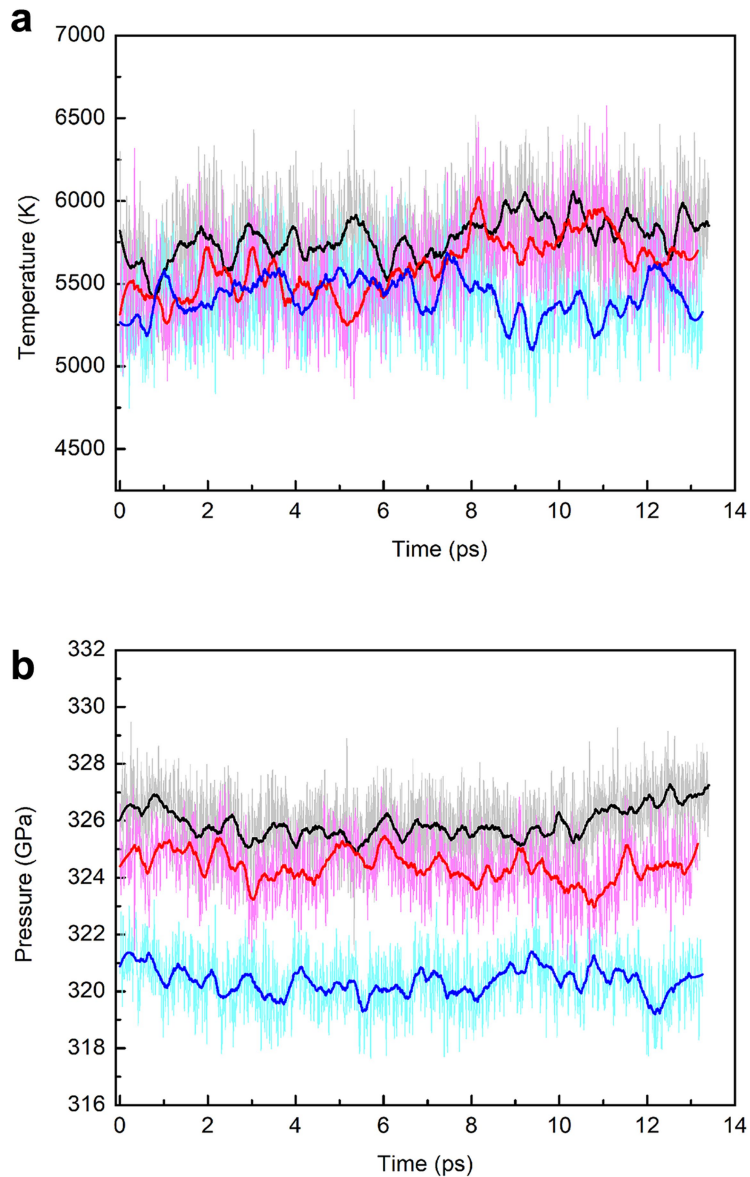
**Peer review information** *Nature* thanks the anonymous reviewers for their contribution to the peer review of this work. Peer reviewer reports are available.

**Reprints and permissions information** is available at <http://www.nature.com/reprints>.



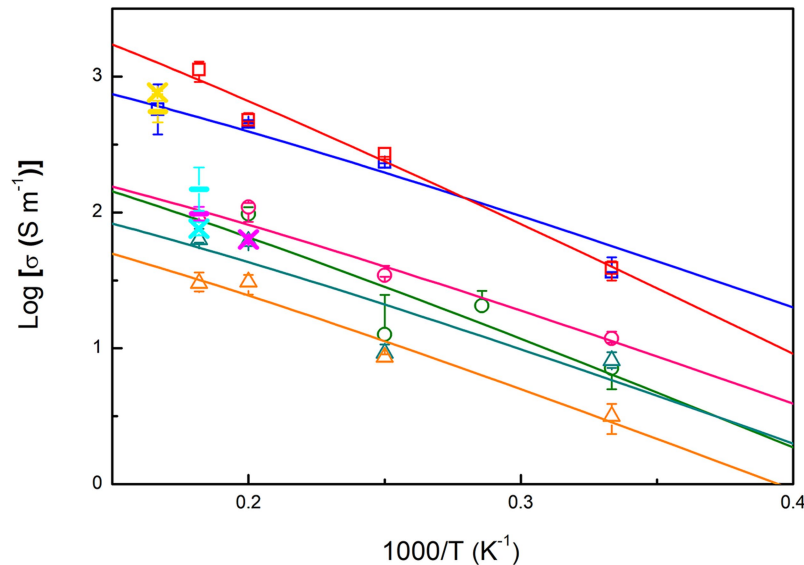
**Extended Data Fig. 1 | Trajectories and mean square displacements (MSDs) of H, O, C and Fe in Fe-light-element alloys.** Trajectories of **a**, H and Fe in FeH<sub>0.25</sub>; **b**, O and Fe in FeO<sub>0.0625</sub>; **c**, C and Fe in FeC<sub>0.0625</sub> at the superionic state

under the IC conditions (~360 GPa and ~5000 K). Small pink, red, black and brown spheres represent the trajectories of H, O, C and Fe, respectively. MSDs of **d**, H and Fe in FeH<sub>0.25</sub>; **e**, O and Fe in FeO<sub>0.0625</sub>; **f**, C and Fe in FeC<sub>0.0625</sub>.



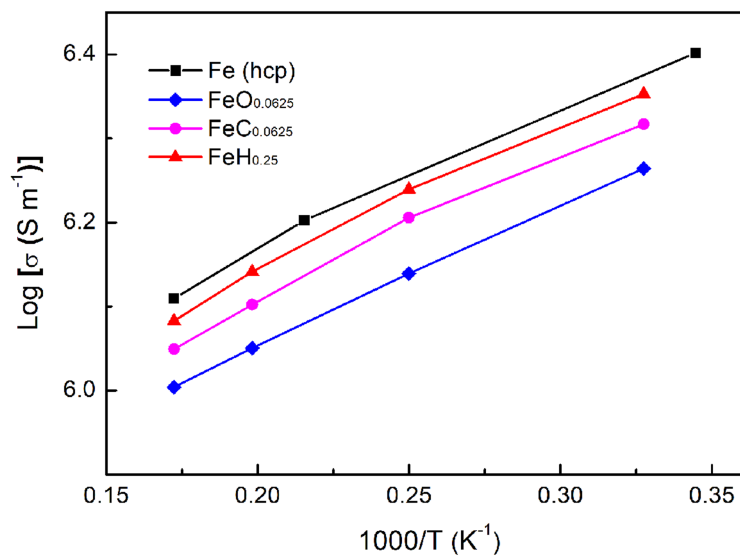
**Extended Data Fig. 2 | The evolution of temperature and pressure with respect to simulation time in the two-phase coexisting systems for Fe-H, Fe-O and Fe-Calloys.** **a**, Temperatures and **b**, pressures for Fe-H, Fe-O and Fe-C

alloys are shown with light grey, pink and cyan curves, and the averaged data over a 0.5 ps period are shown with thick black, red, and blue curves.

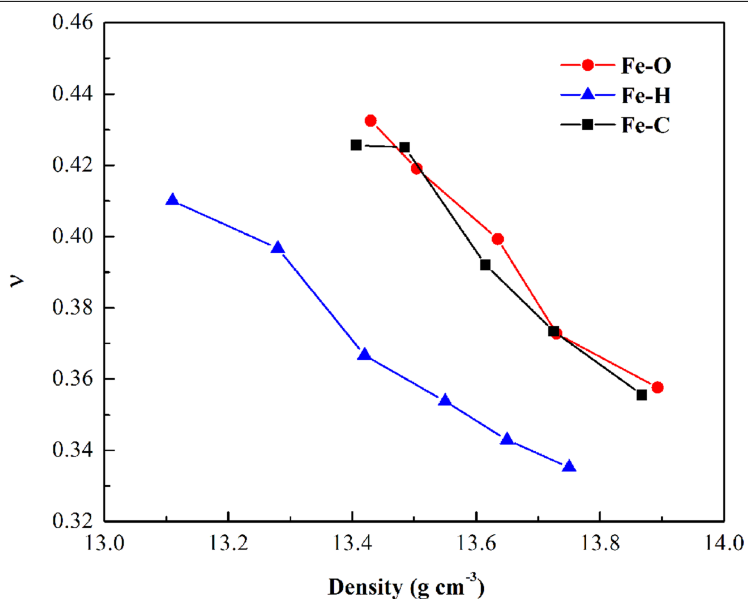


**Extended Data Fig. 3 | Ionic conductivities of superionic Fe alloys at the core conditions.** Diffusion coefficients calculated using  $4 \times 4 \times 2$  supercells and 10 ps simulation time are shown with open symbols. Blue squares:  $\text{FeH}_{0.25}$  at  $-260 \text{ GPa}$ ; red squares:  $\text{FeH}_{0.25}$  at  $-360 \text{ GPa}$ ; cyan triangles:  $\text{FeO}_{0.0625}$  at  $-260 \text{ GPa}$ ; orange triangles:  $\text{FeO}_{0.0625}$  at  $-360 \text{ GPa}$ ; green circles:  $\text{FeC}_{0.0625}$  at  $-260 \text{ GPa}$ ; pink

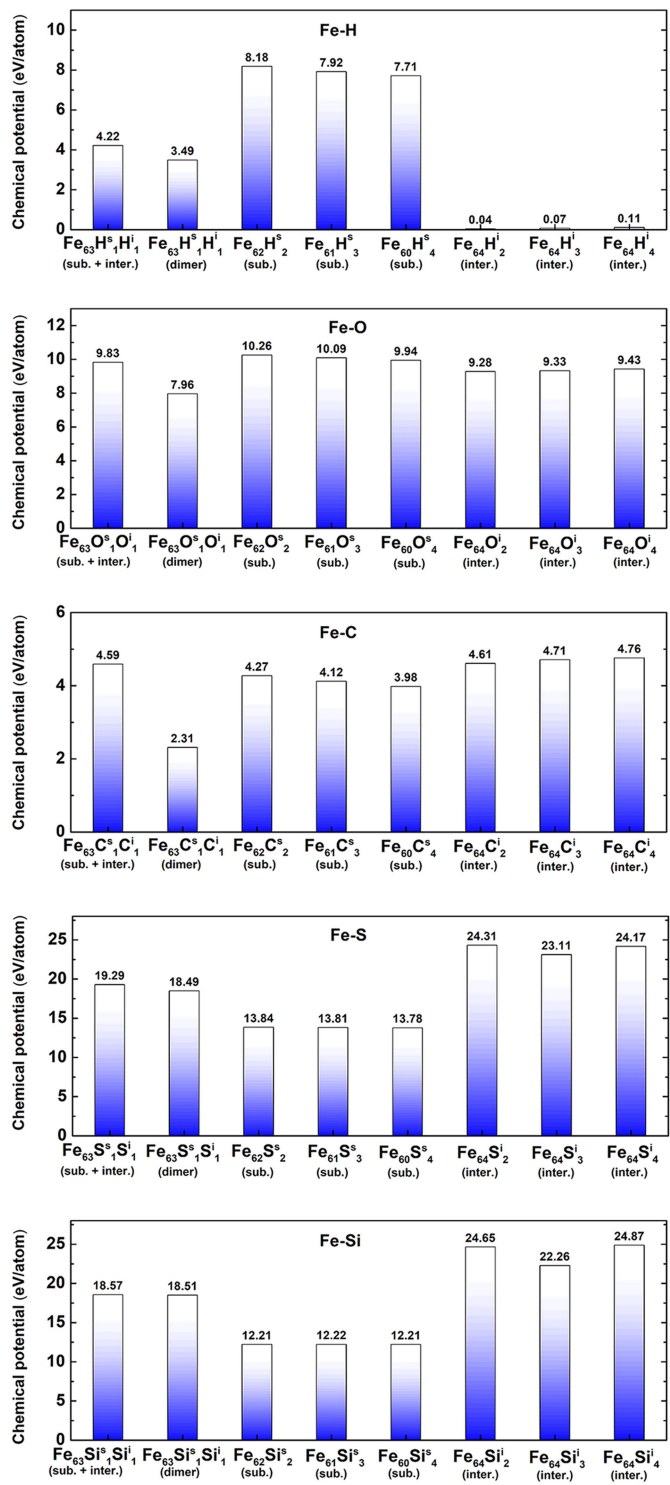
circles:  $\text{FeC}_{0.0625}$  at  $-360 \text{ GPa}$ . The convergence test results using  $4 \times 4 \times 6$  supercell and 100 ps simulation time are labeled by crosses and bars. The results of convergence test are presented with yellow, magenta, and cyan symbols for  $\text{FeH}_{0.25}$ ,  $\text{FeO}_{0.0625}$ , and  $\text{FeC}_{0.0625}$ , respectively.



**Extended Data Fig. 4 | Electronic conductivities of Fe and Fe alloys at 360 GPa with increasing temperature.** The electronic conductivities of Fe,  $\text{FeH}_{0.25}$ ,  $\text{FeO}_{0.0625}$ , and  $\text{FeC}_{0.0625}$  calculated by DFT + DMFT method are shown by black, blue, red, and magenta symbols.

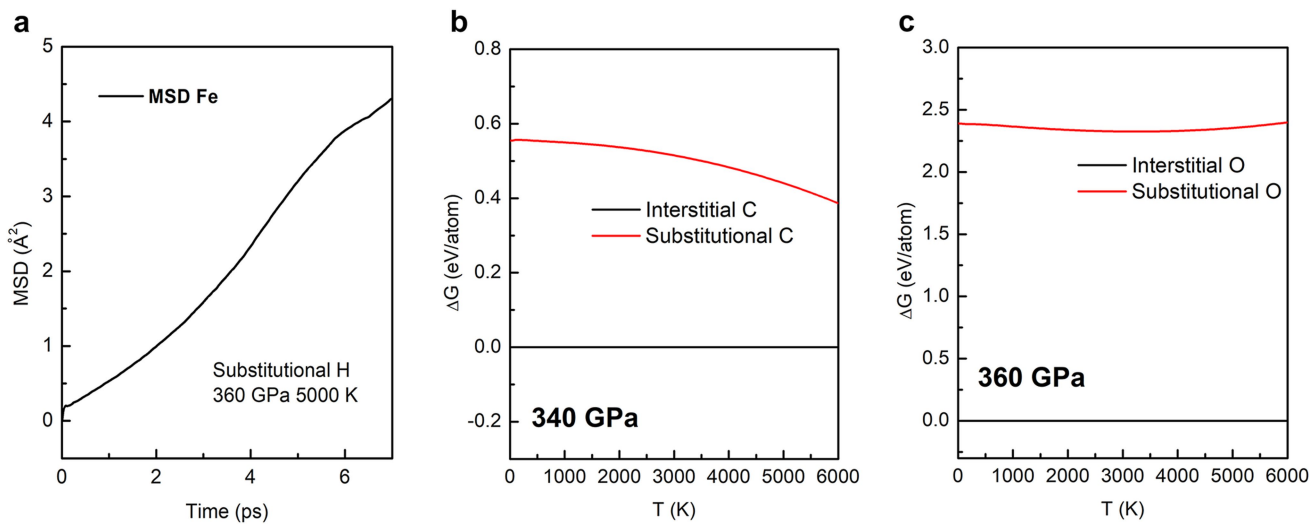


**Extended Data Fig. 5 | Calculated Poisson's ratios of  $\text{FeH}_{0.25}$ ,  $\text{FeC}_{0.0625}$  and  $\text{FeO}_{0.0625}$  at various temperatures and 360 GPa.** Increasing temperature leads to obvious increases in Poisson's ratios approaching the value of the inner core (~0.44).

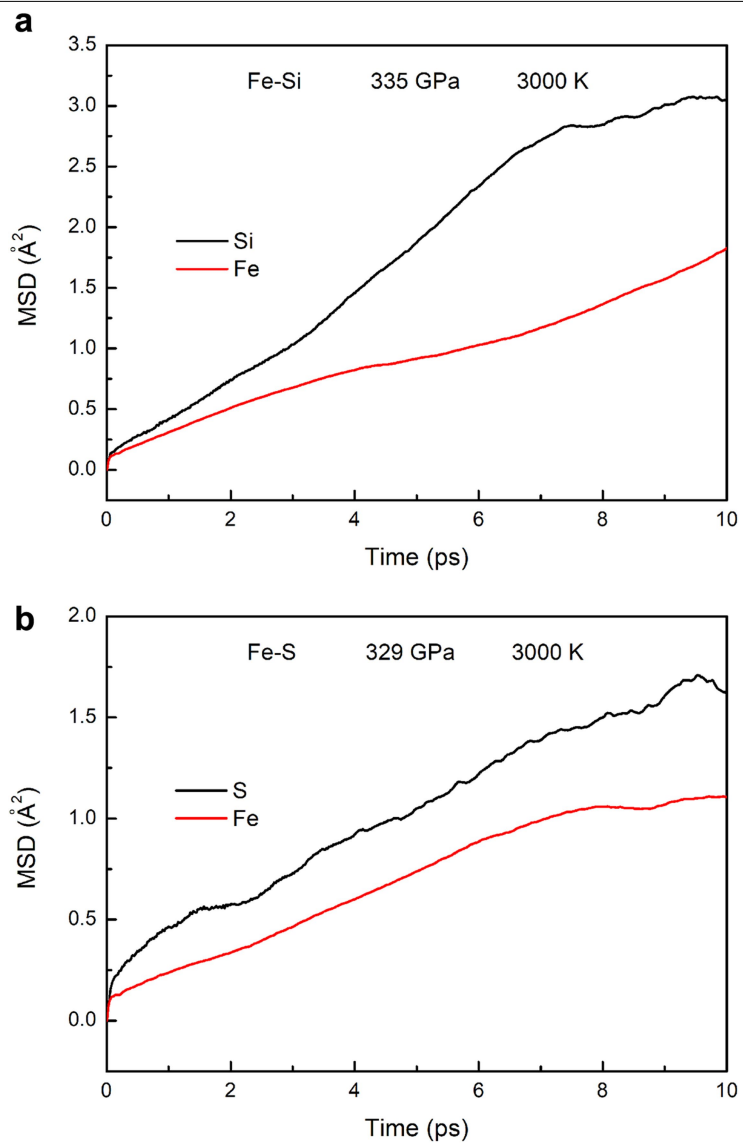


**Extended Data Fig. 6 | Calculated chemical potentials of X (X=H, O, C, S, and Si) in hcp-Fe with different configurations at 360 GPa and 0 K. The chemical potentials are shown with blue bars. The superscripts s and i denote the substitutional and interstitial defects. Separated(sub. + inter.) and correlated (dimer) configurations are noted.**

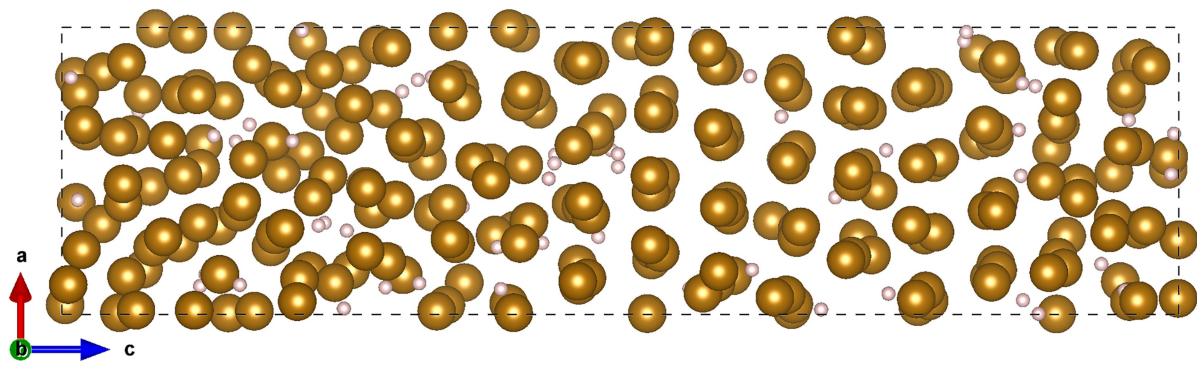
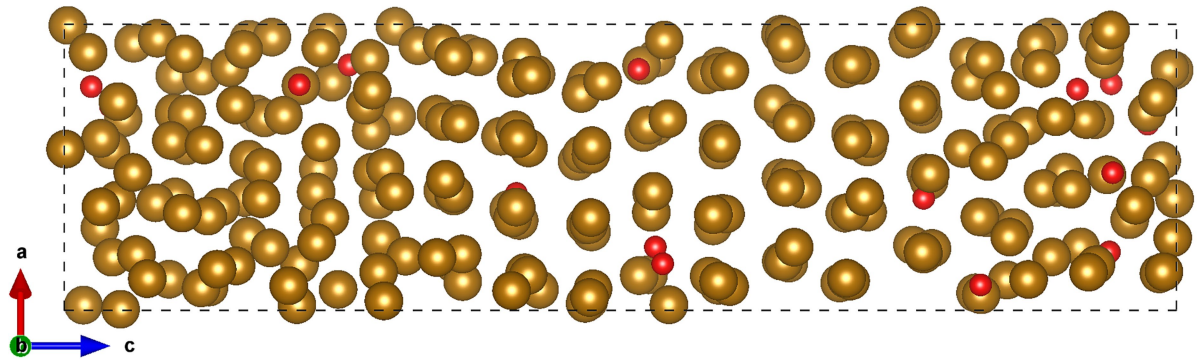
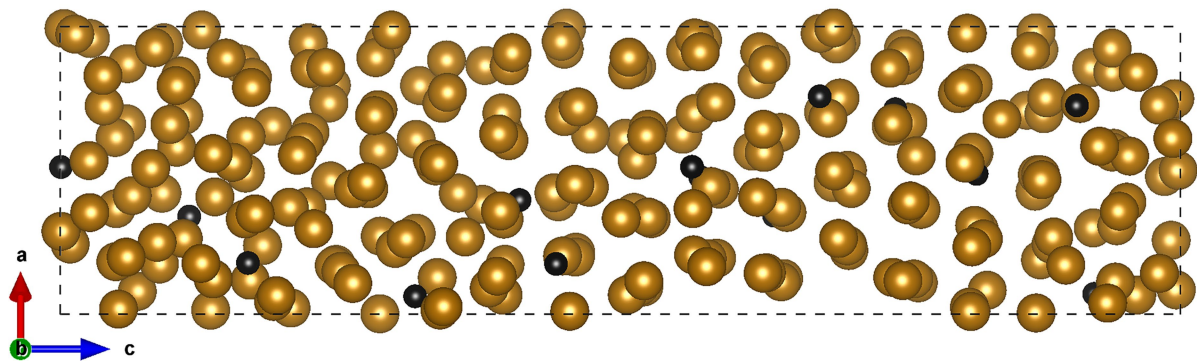
# Article



**Extended Data Fig. 7 | The stability of interstitial and substitutional H, C and O in hcp-Fe under inner core conditions.** **a**, The MSD of Fe in  $\text{Fe}_{60}\text{H}_4$  at 360 GPa and 5000 K; The relative formation energy of **b**, C and **c**, O at interstitial and substitutional site at 340 GPa and 360 GPa, respectively.



**Extended Data Fig. 8 | MSDs of Si, S, and Fe in  $\text{FeSi}_{0.0625}$  and  $\text{FeS}_{0.0625}$  at ~330 GPa and 3000 K.** MSDs of **a**, Si and Fe in  $\text{FeSi}_{0.0625}$ ; **b**, S and Fe in  $\text{FeS}_{0.0625}$ . The MSDs of Si, S and Fe increase obviously with simulation time indicating a liquid state.

$\text{FeH}_{0.25}$  $\text{FeO}_{0.0625}$  $\text{FeC}_{0.0625}$ 

**Extended Data Fig. 9 | The structures of two-phase systems of Fe-H, Fe-O and Fe-C after the AIMD simulations.** These structures suggest the coexistence of solid and liquid Fe alloys. Pink, red, black and brown spheres represent H, O, C and Fe atoms, respectively.

**Extended Data Table 1 | Densities ( $\rho$ ), elastic constants ( $C_{ij}$ ), sound velocities ( $V_\phi$ ,  $V_p$  and  $V_s$ ), moduli (B and G) and Poisson's ratio of  $\text{FeH}_{0.25}$ ,  $\text{FeC}_{0.0625}$  and  $\text{FeO}_{0.0625}$  at various temperatures and 360 GPa**

T(K)		$\rho$	$C_{11}$	$C_{12}$	$C_{13}$	$C_{33}$	$C_{44}$	$V_\phi$	$V_p$	$V_s$	B	G	v
	(K)	(g cm <sup>-3</sup> )	(GPa)	(GPa)	(GPa)	(GPa)	(GPa)	(km s <sup>-1</sup> )	(km s <sup>-1</sup> )	(km s <sup>-1</sup> )	(GPa)	(GPa)	
$\text{FeH}_{0.25}$	0	13.75	2390.3	1201.6	1107.3	2529.3	508	10.69	12.99	6.5	1571.23	581.7	0.335
	2000	13.65	2272.9	1177.9	1085.4	2372.7	458.2	10.53	12.75	6.23	1512.88	530.77	0.343
	3000	13.55	2194.4	1183.6	1070.1	2194.8	394.8	10.42	12.46	5.93	1470.13	476.32	0.354
	4000	13.42	2050.3	1158.5	1073.3	2059	339.6	10.28	12.12	5.56	1418.87	415.32	0.367
	5000	13.28	1868.8	1214.2	1110.8	1829.7	247.5	10.2	11.61	4.81	1381.1	306.56	0.397
	6000	13.11	1732.7	1177.9	1054.2	1684.1	177.8	9.96	11.17	4.37	1302.46	250.81	0.410
$\text{FeC}_{0.0625}$	0	13.87	2275.1	1257	1199.6	2349.9	466.4	10.67	12.71	6.03	1579.17	504.64	0.356
	3000	13.74	1940.7	1168.1	1113.8	2041	361.9	10.15	11.87	5.33	1412.64	390.47	0.373
	4000	13.62	1986.8	1370.5	1053.2	1897.3	274.9	10.23	11.71	4.93	1424.97	331.18	0.392
	5000	13.49	1732	1260.4	1222.7	1705.7	189.9	10.18	11.19	4.05	1397.92	220.71	0.425
	5500	13.41	1687.5	1256.8	1079.7	1590.6	147	9.89	10.87	3.91	1310.89	205.17	0.427
$\text{FeO}_{0.0625}$	0	13.89	2250.7	1257.1	1216.8	2365.3	467.7	10.67	12.66	5.99	1583.12	498.17	0.358
	3000	13.73	2095.7	1123.7	1209.9	2038.9	338.1	10.38	12.16	5.47	1479.7	411.56	0.373
	4000	13.64	1902.3	1219.3	1228.6	1907.2	273.6	10.32	11.71	4.79	1451.64	313.43	0.400
	5000	13.50	1807.3	1307	1117.2	1652.6	174.3	10.08	11.17	4.17	1372.22	234.81	0.419
	5500	13.43	1675.6	1226.5	1227	1692.5	147.7	10.13	11.04	3.81	1378.3	194.86	0.432